

Angular distributions of antiprotons elastically and inelastically scattered by helium

James S. Cohen*

Theoretical Division, Los Alamos National Laboratory, Los Alamos, New Mexico 87545, USA

(Received 30 April 2008; revised manuscript received 23 June 2008; published 21 July 2008)

Angular differential cross sections are calculated for antiprotons elastically and inelastically scattered by the helium atom. The elastic cross sections are calculated quantum mechanically using both the adiabatic potential and a phenomenological optical potential. The absorptive effects, taken into account by the optical potential, are found to significantly suppress large-angle elastic scattering. Inelastic scattering (excitation and ionization) is treated by the quasiclassical fermion molecular dynamics method. The inelastic scattering is largely in the backward direction at laboratory collision energies within ~ 30 eV of threshold, but moves to smaller angles as the energy increases.

DOI: 10.1103/PhysRevA.78.012509

PACS number(s): 36.10.-k, 34.50.Cx, 25.43.+t

I. INTRODUCTION

Now that antiprotons have been trapped [1–3], experiments to use them for scattering as well as antimatter formation are planned [4,5]. In order to design relevant \bar{p} detectors, prior estimates of the angular distributions are needed. In particular, some of the proposed experiments will be with the atomic helium target [6], in which the \bar{p} may be captured as well as be elastically or inelastically scattered. In the present work, the angular differential cross sections for elastic scattering are calculated quantum mechanically and the angular differential cross sections for inelastic collisions are calculated using a quasiclassical method previously used for \bar{p} capture [7].

Unlike the atomic H target, for which a critical distance exists inside which an adiabatic potential curve is undefined, an adiabatic potential curve is defined for all \bar{p} -He distances. The usual procedure for calculating an elastic scattering cross section at low energies is by solution of the single-channel Schrödinger equation using this potential curve. However, it is known that the capture and ionization cross sections for \bar{p} -He collisions are large at low energies in spite of the absence of a critical distance [8]. Thus the usual approach may not be adequate. In the present work, \bar{p} -He elastic scattering is treated as usual, as well as by solving the complex Schrödinger equation with an optical potential, and the results are compared.

II. DIFFERENTIAL ELASTIC SCATTERING

A. Calculation with adiabatic potential

The Born-Oppenheimer potential curves $V_a(R)$ for \bar{p} +He, calculated by Todd and Armour [9] and by Gibbs [10], are shown in Fig. 1. For the present work the former curve is adopted, slightly modified at $R \geq 10a_0$ to make it agree with the accurate polarization potential, $V_a(R) \sim -\alpha/2R^4$ where $\alpha = 1.383\,174$ [11].¹

The scattering is treated quantum mechanically by solving the time-independent Schrödinger equation in the center-of-mass system,

$$\left(-\frac{1}{2\mu}\nabla^2 + V_a(R) - E_{c.m.}\right)F(R) = 0, \quad (1)$$

where μ is the reduced mass of \bar{p} +He and $F(R)$ is the wave function describing the relative motion for energy $E_{c.m.}$. A partial-wave expansion of $F(R)$,

$$F(R) = R^{-1} \sum_{l=0}^{\infty} u_l(R) P_l(\cos \theta_{c.m.}), \quad (2)$$

results in the radial equations

$$\left(\frac{d^2}{dR^2} - \frac{l(l+1)}{R^2} + 2\mu[E_{c.m.} - V_a(R)]\right)u_l(R) = 0. \quad (3)$$

The asymptotic form

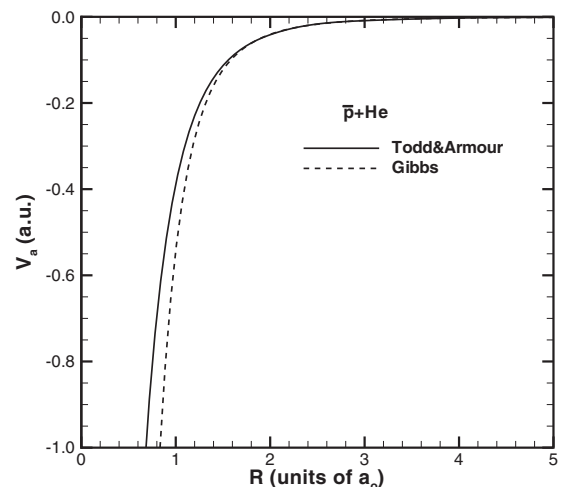


FIG. 1. Accurate adiabatic potential of Todd and Armour [9] and smaller calculation of Gibbs [10].

*cohen@lanl.gov

¹Atomic units are used except where specified otherwise.

$$u_l(R) \sim \sin\left(kR - \frac{1}{2}l\pi + \eta_l\right), \quad (4)$$

where $k=(2\mu E_{\text{c.m.}})^{1/2}$, defines the partial-wave phase shift η_l , in terms of which the differential angular cross section is given by

$$\left(\frac{d\sigma}{d\Omega}\right)_{\text{c.m.}} = \frac{1}{4k^2} \left| \sum_{l=0}^{\infty} (2l+1)(e^{2i\eta_l} - 1)P_l(\cos\theta_{\text{c.m.}}) \right|^2 \quad (5)$$

and the integrated cross section by

$$\sigma = \frac{4\pi}{k^2} \sum_{l=0}^{\infty} (2l+1)\sin^2 \eta_l. \quad (6)$$

The differential cross section in the laboratory system depends on the projectile-to-target mass ratio $\gamma=m_p/m_{\text{He}}$. It is assumed that the initial motion of the helium atom can be neglected. The laboratory differential cross section, at angle

$$\theta_{\text{lab}} = \tan^{-1}\left(\frac{\sin\theta_{\text{c.m.}}}{\gamma + \cos\theta_{\text{c.m.}}}\right), \quad (7)$$

is related to the cross section in the c.m. system by [12]

$$\left(\frac{d\sigma}{d\Omega}\right)_{\text{lab}} = \frac{(\gamma^2 + 2\gamma \cos\theta_{\text{c.m.}} + 1)^{3/2}}{\gamma \cos\theta_{\text{c.m.}} + 1} \left(\frac{d\sigma}{d\Omega}\right)_{\text{c.m.}}. \quad (8)$$

Of course, the integrated cross section must be the same in the laboratory and center-of-mass systems.

The resulting differential cross sections are shown by the red (or gray) curves in Fig. 2 for several collision energies between 10 and 300 eV in the laboratory frame. As usual, they are strongly peaked in the forward direction and, at the lower energies, also peak in the backward direction. To aid in interpretation of the backward peak, the absolute phase shifts were also calculated in the WKBJ approximation (solution of the Schrödinger equation gives the phase shifts only modulo π), in terms of which the classical deflection angle ϑ is given by

$$\vartheta\left(l + \frac{1}{2}\right) = 2\frac{\partial\eta_l}{\partial l}. \quad (9)$$

In the range of energies calculated, the classical deflection angle is found to have an extremum between $l=18$ and 20. For $E_{\text{lab}} \lesssim 40$ eV the magnitudes of these extrema exceed π radians, thus yielding a distinct peak in the backward direction (“glory” scattering) [13]. At higher energies, the classical deflection angle does not exceed π and the backward peak vanishes. In addition, rapid oscillations can be seen due to interference between the two trajectories on opposite sides of the extrema where ϑ is the same for two different values of l , whether or not the phase shifts exceed π . The effects of interference are more prominent at low energies where the wavelengths are longer.

B. Calculation with an optical potential

In the optical-potential description, the adiabatic potential $V_a(R)$ is replaced by the complex potential

$$W(R) = V_a(R) + \Delta V(R) - \frac{1}{2}i\Gamma(R), \quad (10)$$

where $\Delta V(R)$ is a shift and $\Gamma(R)$ is a width. Formally, the formulations of the scattering equation and phase shift are the same as in the adiabatic description in Sec. II A, except all quantities are complex. However, it is generally more convenient to separate the real and imaginary parts in route to defining the elastic and nonelastic cross sections, and this approach will be taken here. The resulting phase shift is complex and can be written

$$\eta_l = \eta_l^{(r)} + i\eta_l^{(i)}, \quad (11)$$

where $\eta_l^{(r)}$ and $\eta_l^{(i)}$ are real. The same formulas given in Sec. II A for the elastic cross sections still apply, although it is now more transparent to write the integrated elastic cross section as

$$\sigma_{el} = \frac{2\pi}{k^2} \sum_{l=0}^{\infty} (2l+1) [\cosh(2\eta_l^{(i)}) - \cos(2\eta_l^{(r)})] e^{-2\eta_l^{(i)}}. \quad (12)$$

The nonelastic cross section includes capture as well as scattering with ionization or excitation, but its components are not separated. The total nonelastic cross section is given by

$$\sigma_{ne} = \frac{\pi}{k^2} \sum_{l=0}^{\infty} (2l+1) [1 - e^{-4\eta_l^{(i)}}]. \quad (13)$$

Of course, no particle is scattered in the case of capture, so this procedure is not generally suitable for calculating an inelastic differential cross section.

The imaginary component of the phenomenological optical potential is determined such that the resulting nonelastic cross sections approximately match the energy-dependent nonelastic cross sections determined by the fermion molecular dynamics (FMD) method [14] (see Sec. III). The FMD cross section is consistent with capture ratios determined experimentally in helium mixtures [15]. It was found adequate to take this imaginary potential, which is half the autoionization width, as independent of energy. The width is determined by the magnitude and the impact-parameter (partial wave in the quantum-mechanical formulation) dependence of the nonelastic cross sections (see the Appendix for details). The simple Gaussian form

$$\Gamma = ce^{-(R/b_0)^2}, \quad (14)$$

with $b_0=0.40a_0$ and $c=0.92$ a.u., shown in Fig. 3, was found to be adequate at the considered energies.

This phenomenological width is significantly smaller than a diabatic width previously determined [16] using a frozen-orbital description of the $\bar{p}+\text{He}$ interaction, shown for comparison in Fig. 3, thus demonstrating that relaxation effects are important. It should be noted that the optical-potential description, at least with the assumption of energy independence, is not valid for higher-energy ($E_{\text{c.m.}} \gtrsim 100$ eV) collisions where the effects of dynamical couplings become important.

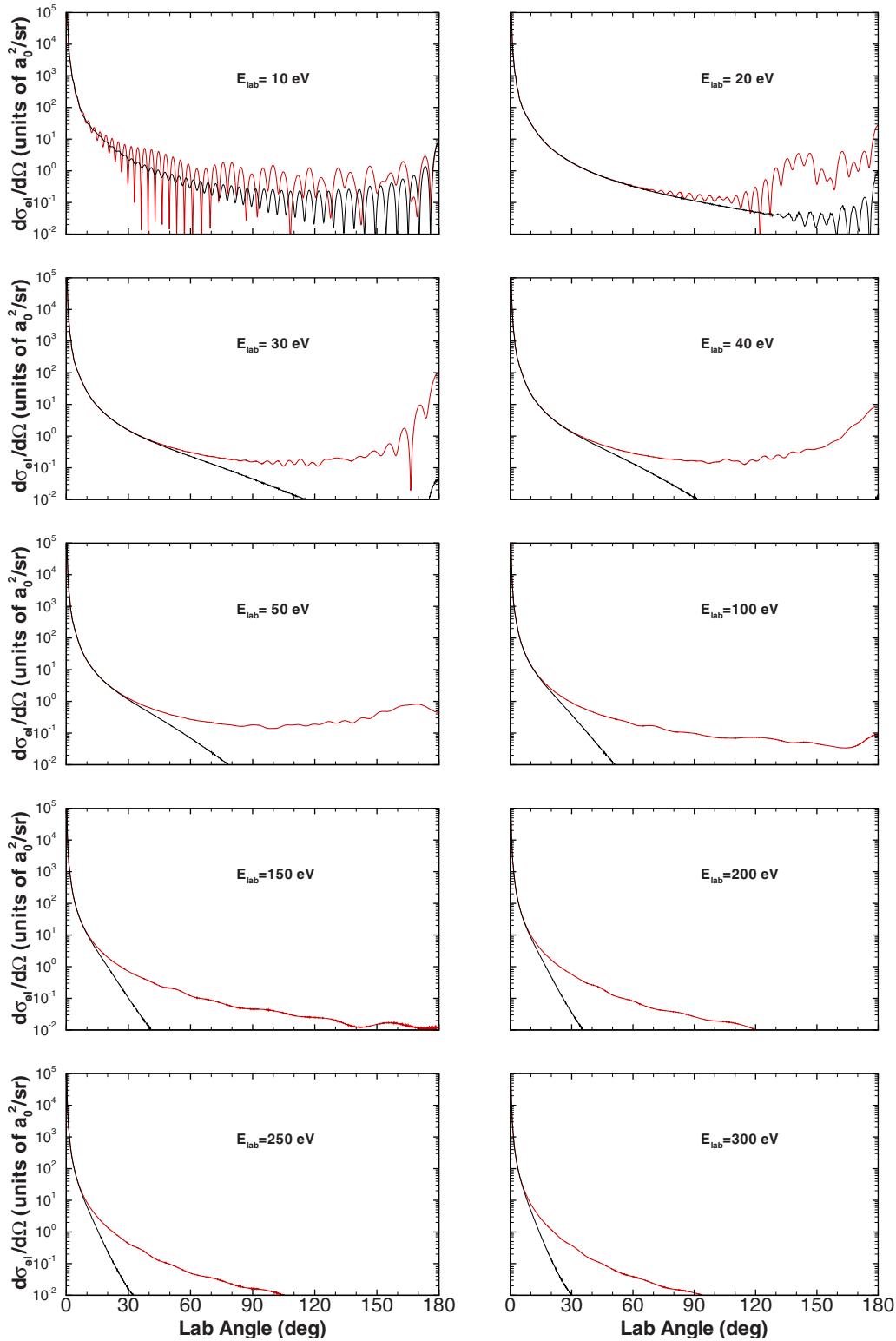


FIG. 2. (Color online) Angular differential elastic cross sections for $\bar{p}+\text{He}$, calculated by solution of the Schrödinger equation using the adiabatic potential [red (gray)] and optical potential (black). The optical-potential calculation should be more realistic.

The real part of the potential is taken to be the same as the adiabatic potential used in Sec. II A. Really this real part is subject to an energy shift, which can be expected to be of the same order of magnitude as the width. The neglect of this shift can thus be retroactively justified since the width is

found to be small compared with the real potential, as can be seen by comparing Figs. 1 and 3. This relationship is especially true since the width becomes very small at $R \geq 0.5a_0$ while the magnitude of the real potential increases as R^{-1} at smaller R .

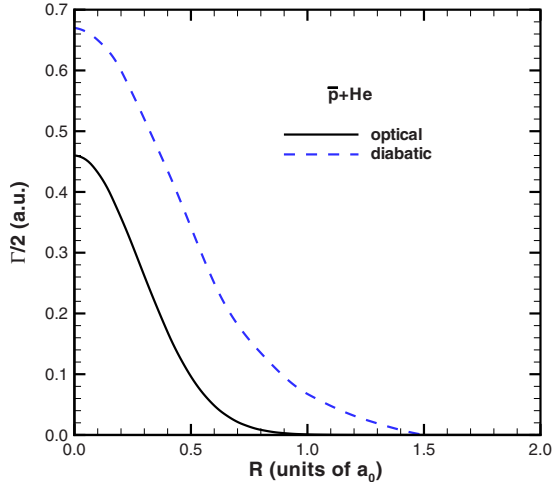


FIG. 3. (Color online) Imaginary part of the energy-dependent optical potential. The present value calculated by fitting the non-elastic FMD cross sections is shown by the solid curve ; the result previously calculated using a frozen-orbital diabatic description [16] is shown by the dashed curve.

The differential elastic cross sections calculated with the optical potential are shown in Fig. 2 as black curves. The scattering is little affected by the imaginary part at small angles, which generally come from large impact parameters where the interaction is weak. However, large-angle scattering is significantly suppressed, especially at collision energies above the target ionization potential. The interference oscillations persist at the higher energies, but their amplitudes are reduced.

The corresponding integrated elastic cross sections are shown in Fig. 4. The integrated cross sections calculated by the adiabatic- and optical-potential descriptions are roughly parallel, with the optical-potential result always slightly smaller.

To explicitly demonstrate that the effect of the undetermined shift can be expected to be small, some calculations

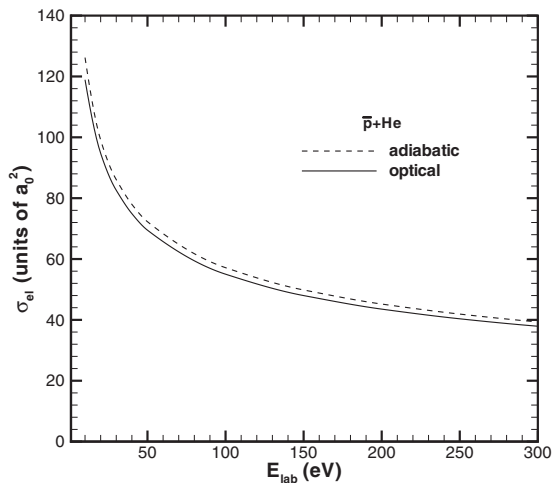


FIG. 4. Integrated elastic cross sections for $\bar{p} + \text{He}$, calculated by solution of the Schrödinger equation using the adiabatic potential (dashed curve) and the optical potential (solid curve). The optical-potential calculation should be more realistic.

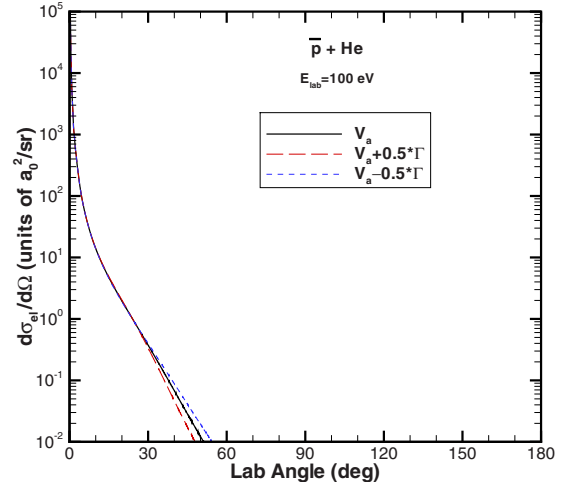


FIG. 5. (Color online) Possible effect of undetermined shift on the elastic $\bar{p} + \text{He}$ cross section at collision energy 100 eV. The long- and short-dashed curves show the modifications of the cross sections due to an increase and decrease, respectively, of the adiabatic potential by half the width.

were repeated with the real potential shifted up and down within the width. The effects on the differential cross section at 100 eV are shown in Fig. 5. The resulting changes at small scattering angles are negligible, and the changes at large angles are still reasonably small. Thus the expectation that the adiabatic potential suffices as the *real* part is verified.

III. DIFFERENTIAL INELASTIC SCATTERING

A variety of methods have been used to calculate the cross sections for capture of an antiproton (or similarly behaving negative muon), though complete quantum-mechanical calculations have not yet succeeded. Perturbative methods fail, but the various nonperturbative methods are in fairly good agreement [8]. Capture by atoms is due almost entirely to ionization—of a single electron in the case of helium. Thus the capture cross section decreases sharply at energies exceeding the first ionization potential of the target helium atom, though the sum of the ionization and capture cross sections displays smooth behavior at this point. The quasiclassical FMD method is used here. The FMD method has been successful in calculating the \bar{p} capture cross sections for helium as well as for heavier multielectron atoms, in which multiple ionization can be important, though angular differential cross sections have not previously been reported. Of importance for this purpose, linear and angular momenta as well as energy are accurately conserved in the FMD treatment.

The FMD method [14] utilizes the Kirschbaum-Wilets ansatz for atomic structure [17]. In this model, pseudopotentials V_H and V_P constrain the quasiclassical dynamics to satisfy the Heisenberg uncertainty and Pauli exclusion principles, respectively. The resulting multielectron atoms, which do not exist classically, are stable and possess shell structures, though the shells obtained are not entirely faithful to the real atoms [18]. Similar terms are included for the

exotic atom structure, but have little effect since it is formed in highly excited states which behave nearly classically according to the correspondence principle.

The FMD effective Hamiltonian for the system is written

$$H_{\text{FMD}} = H_0 + V_H + V_P, \quad (15)$$

where H_0 is the usual Hamiltonian of the system containing the kinetic energies of all particles and the Coulomb potentials between all pairs of particles. The extra terms are of the form

$$V_H = \sum_{i=1}^{N_e} \frac{\hbar^2}{\mu_{ni} r_{ni}^2} f(r_{ni} p_{ni}; \xi_H, \alpha_H) + \frac{\hbar^2}{\mu_{n\bar{p}} r_{n\bar{p}}^2} f(r_{n\bar{p}} p_{n\bar{p}}; \xi_H, \alpha_H) \quad (16)$$

and

$$V_P = \sum_{i=1}^{N_e} \sum_{j=i+1}^{N_e} \frac{\hbar^2}{\mu_{ij} r_{ij}^2} f(r_{ij} p_{ij}; \xi_P, \alpha_P) \delta_{s_i, s_j}, \quad (17)$$

where the sums are over the N_e electrons, r_{ni} (p_{ni}) is the relative distance (momentum) of electron i with respect to the nucleus n , $r_{n\bar{p}}$ ($p_{n\bar{p}}$) is the relative distance (momentum) of the \bar{p} with respect to the nucleus n , r_{ij} (p_{ij}) is the relative distance (momentum) of electron j with respect to electron i , μ designates the reduced mass of the subscripted particles, and s_i (s_j) is the spin of electron i (j). Hamilton's classical equations of motion are solved with the Hamiltonian H_{FMD} .

The constraining potentials are implemented by the form [17]

$$f(rp; \xi, \alpha) \equiv \frac{\xi^2}{4\alpha} \exp\left\{ \alpha \left[1 - \left(\frac{rp}{\xi\hbar} \right)^4 \right] \right\}, \quad (18)$$

where the dimensionless parameter ξ reflects the size of the core and α its hardness. The values $\xi_H = 0.9343$ and $\alpha_H = 2.0$ are used for helium [7]; the Pauli term vanishes for the ground-state helium target since its two electrons have opposite spins.

The calculation of each trajectory proceeds in three steps: (i) choose initial conditions (\mathbf{r}_0 and \mathbf{p}_0 for all particles), (ii) integrate Hamilton's classical equations of motion, and (iii) examine the asymptotic trajectory for the final state. These steps are repeated a sufficient number of times to get good statistics for the process "R" of interest. The corresponding cross section is given by

$$\sigma_R = \frac{N_R}{N_{\text{tot}}} \pi b_{\text{max}}^2, \quad (19)$$

where the process R is found to occur N_R times in N_{tot} total trajectories, chosen with b statistically sampled in the range $(0, b_{\text{max}})$ (in practice, this sampling is done in segments, so b_{max} need not be known in advance). The calculation of the differential inelastic cross section is similar to that previously done for \bar{p} capture [7] except much larger numbers of trajectories ($\sim 100\,000$ at each energy) were employed in order to obtain smooth converged cross sections. The angular distributions are placed in histograms with bin sizes chosen such that smooth fits are possible.

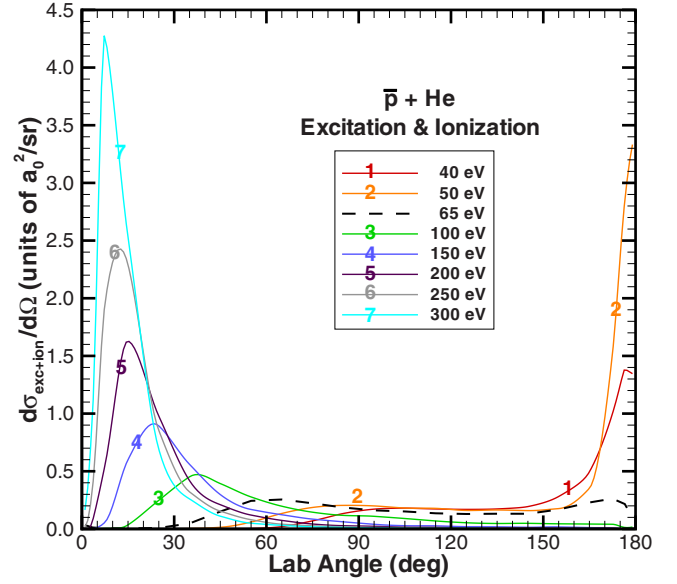


FIG. 6. (Color online) Angular differential inelastic (excitation + ionization) cross sections, calculated by the FMD method. The crossover between predominance of scattering into the forward and backward hemispheres occurs at ~ 65 eV (cross section shown by the dashed curve).

The results are shown in Fig. 6. The inelastic angular distributions are strongly backward peaked at the lowest two energies, where only the hardest collisions can ionize or excite the target. As the incident energy increases, the peaks in the differential cross sections move to smaller angles. At a collision energy of ~ 65 eV the forward and backward hemispheres are of about equal importance.

The component integrated cross sections are shown in Fig. 7. The integrated cross section for \bar{p} inelastically scattered is the sum of its ionization and excitation components, although there is relatively little excitation in the energy

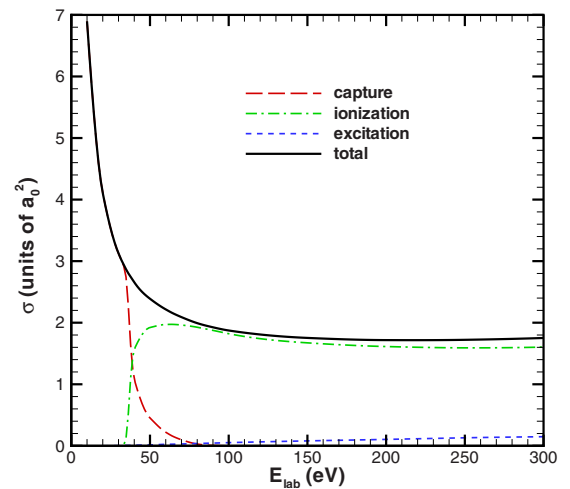


FIG. 7. (Color online) Capture (long-dashed curve), ionization (dot-dashed curve), excitation (short-dashed curve), and the total nonelastic (solid curve) cross sections for $\bar{p} + \text{He}$ collisions. The integrated results of the differential cross sections shown in Fig. 6 are given by the sum of the ionization and excitation cross sections.

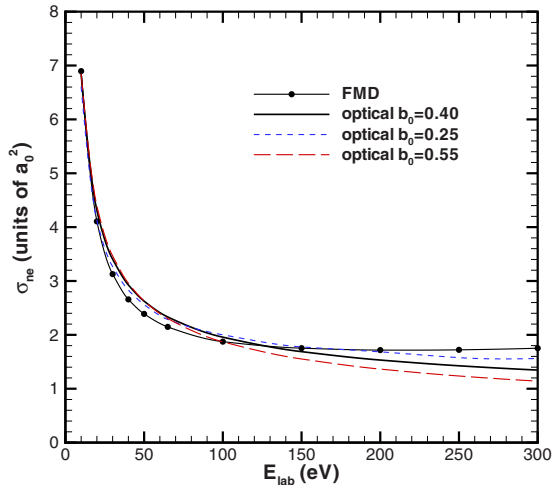


FIG. 8. (Color online) Total nonelastic (capture+ionization +excitation) cross section calculated by the FMD method (solid curve with data points) and quantum mechanically with the phenomenological optical potential (solid curve) shown in Fig. 3 as well as with two variant optical potentials (dashed curves).

range considered. It is the total of these nonelastic cross sections that goes into the determination of the width (see the Appendix). We also note that double ionization by scattered \bar{p} in this energy range is found to be relatively rare ($<1\%$ of all ionizations). However, capture of the \bar{p} almost invariably results in both electrons ultimately being ionized.

IV. CONCLUSIONS

Unlike scattering of protons by atoms and molecules, scattering of antiprotons cannot be expected to be adiabatic at low collision energies. Ionization of the target can generally occur even at energies just slightly above the threshold, and capture to form an antiprotonic atom can generally occur even in zero-energy collisions. Thus elastic scattering is affected even at very low energies, and the usual adiabatic treatment will never become accurate. The optical-potential treatment is useful for such collisions, except at extremely low collision energies [19], and has been used in the present work. Calculations were done at energies relevant to planned experiments, 10–300 eV [6]. At large angles, decreasing as the collision energy increases, inelastic scattering dominates. The inelastic cross section does not include capture, which dominates at collision energies below about 30 eV (near the threshold collision energy required to ionize helium), since in this case no antiproton is scattered.

ACKNOWLEDGMENTS

I would like to thank Professor Y. Yamazaki for suggesting this problem. This work was done under the auspices of the (U.S.) Department of Energy.

APPENDIX: DETERMINATION OF THE WIDTH FOR THE OPTICAL POTENTIAL

The width for the phenomenological optical potential, assuming the adiabatic potential for the real part, was obtained

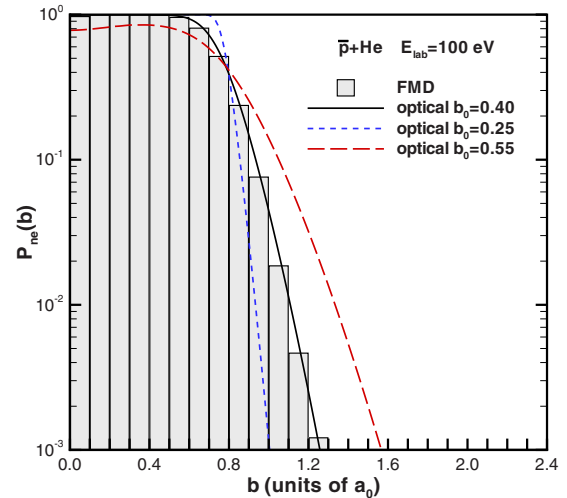


FIG. 9. (Color online) Impact-parameter dependence of the total nonelastic cross section for $\bar{p}+\text{He}$ collisions at 100 eV. The bars show the results of the FMD calculation. The solid curve shows the quantum-mechanical result with the chosen phenomenological optical potential [Eq. (14) with $b_0=0.40$, $c=0.92$]. The dashed curves show the results with variant widths. All three optical potentials give similar integrated cross sections, as shown in Fig. 8.

by determining the values of b_0 and c in Eq. (14) that best fit the FMD total nonelastic cross sections and their impact-parameter dependence in the energy range of interest. The cross sections were calculated quantum mechanically with the optical potential as described in Sec. II B. It was first found that the total cross section could be fit reasonably well with a large range of values of b_0 as long as the corresponding value $c \approx 0.034 \exp[(0.728/b_0)^2]$ was used, as shown in Fig. 8. The impact-parameter dependence then determines the value of b_0 . The best fit was obtained with $b_0=0.40a_0$ and $c=0.92$ a.u. The resulting impact-parameter [given by $b=(l+0.5)/(2\mu E_{c.m.})^{1/2}$] dependence is shown in Fig. 9 for scattering at 100 eV. For comparison, the results with two variant widths $b_0=0.25$ and 0.55 (and the optimal associated values of c) are also shown.

At the shown scattering energy of 100 eV, approximately half of the nonelastic cross section comes from small impact parameters where P_{ne} is essentially unity and the other half from larger impact parameters where P_{ne} is smaller. At lower energies an increasing fraction of the nonelastic cross section comes from impact parameters where $P_{ne} \approx 1$, approaching a step function at $E_{lab} < 10$ eV. At $E_{lab} > 100$ eV the tail of the impact-parameter distribution becomes more significant, but the neglect of the energy dependence of the width also becomes less valid.

Significant further improvement in the fit would probably require inclusion of a (positive) shift in the real part of the potential, but was considered unnecessary for the present work considering the uncertainty in the FMD cross sections and the expected relatively weak dependence of the elastic cross sections on the shift as shown in Fig. 5.

- [1] M. Amoretti *et al.*, *Nature (London)* **419**, 456 (2002).
- [2] G. Gabrielse *et al.*, *Phys. Rev. Lett.* **89**, 213401 (2002).
- [3] G. Gabrielse *et al.*, *Phys. Rev. Lett.* **100**, 113001 (2008).
- [4] Y. Yamazaki, *Nucl. Instrum. Methods Phys. Res. B* **154**, 174 (1999).
- [5] Y. Yamazaki, *Hyperfine Interact.* **138**, 141 (2001).
- [6] Y. Yamazaki (private communication).
- [7] J. S. Cohen, *Phys. Rev. A* **62**, 022512 (2000).
- [8] J. S. Cohen, *Rep. Prog. Phys.* **67**, 1769 (2004).
- [9] A. C. Todd and E. A. G. Armour, *J. Phys. B* **38**, 3367 (2005).
- [10] W. R. Gibbs, *Phys. Rev. A* **56**, 3553 (1997).
- [11] M. Masili and A. F. Starace, *Phys. Rev. A* **68**, 012508 (2003).
- [12] E. W. McDaniel, *Collision Phenomena in Ionized Gases* (Wiley, New York, 1964).
- [13] K. W. Ford and J. A. Wheeler, *Ann. Phys. (N.Y.)* **7**, 259 (1959).
- [14] L. Wilets and J. S. Cohen, *Contemp. Phys.* **39**, 163 (1998).
- [15] J. S. Cohen, *Phys. Rev. A* **65**, 052714 (2002).
- [16] J. S. Cohen, R. L. Martin, and W. R. Wadt, *Phys. Rev. A* **24**, 33 (1981).
- [17] C. L. Kirschbaum and L. Wilets, *Phys. Rev. A* **21**, 834 (1980).
- [18] J. S. Cohen, *Phys. Rev. A* **57**, 4964 (1998).
- [19] A. Yu. Voronin, *Zh. Eksp. Teor. Fiz.* **102**, 760 (1992) [*Sov. Phys. JETP* **75**, 416 (1992)].